Application of Machine Learning to Investigation of Heat and Mass Transfer Over a Cylinder Surrounded by Porous Media-The Radial Basic Function Network

Rasool Alizadeh[1], Javad Mohebbi Najm Abad[2*], Abolfazl Fattahi[3], Ebrahim Alhajri[4], Nader Karimi[5*]
[1]Department of Mechanical Engineering, Quchan Branch, Islamic Azad University, Quchan, Iran
[2]Department of Computer Engineering, Quchan Branch, Islamic Azad University, Quchan, Iran
[3]Department of Mechanical Engineering, University of Kashan, Kashan, Iran
[4]Department of Mechanical Engineering, Khalifa University, Abu Dhabi, UAE
[5]School of Engineering and Materials Science, Queen Mary University of London, London E1 4NS, United Kingdom

*Corresponding author, email: n.karimi@qmul.ac.uk

Abstract
This paper investigates heat and mass transport around a cylinder featuring non-isothermal homogenous and heterogeneous chemical reactions in a surrounding porous medium. The system is subject to an impinging flow while local thermal non-equilibrium, non-linear thermal radiation within the porous region and the temperature dependency of the reaction rates are considered. Further, non-equilibrium thermodynamics including Soret and Dufour effects are taken into account. The governing equations are numerically solved using a finite difference method after reducing them to a system of non-linear ordinary differential equations. Since the current problem contains a large number of parameters with complex inter-connections, low-cost models such as those based on artificial intelligence are desirable for conduction of extensive parametric studies. Therefore, the simulations are used to train an artificial neural network. Comparing various algorithms of artificial neural network, the radial basic function network is selected. The results show that variations in radiative heat transfer as well as those in Soret and Dufour effects can significantly change the heat and mass transfer responses. Within the investigated parametric range, it is found that the diffusion mechanism is dominantly responsible for heat and mass transfer. Importantly, it is noted that the developed predictor algorithm offers a considerable saving of the computational burden.

Keywords: Machine learning; artificial neural network; Nonlinear thermal radiation, Forced convection, Homogenous and heterogeneous reactions, Porous Media.

Nomenclature

a	cylinder radius	q_m	mass flux on the wall
a_{sf}	interfacial area per unit volume of porous media	r	radial coordinate
Bi	Biot number $Bi = \frac{h_{sf} a_{sf}.a}{4k_s}$	Re	Freestream Reynolds number $Re = \frac{\bar{k}.a^2}{2\upsilon}$
C	fluid concentration	R_d	radiation parameter $R_d = \frac{16\sigma^* T_\infty^3}{3k^*.k_s}$
C_p	specific heat at constant pressure	μ_i	center of region
C_s	concentration	σ_i	width of the receptive field
D	molecular diffusion coefficient	Sr	Soret number $Sr = \frac{D.k_f}{T_\infty}\frac{(T_w - T_\infty)}{C_\infty.\alpha}$
Df	Dufour number $Df = \frac{D.k_f}{C_s.C_p}\frac{C_\infty}{(T_w - T_\infty)\upsilon}$	Sh	Sherwood number
E	non-dimensional energy of activation $E = \frac{E_a}{k.T_\infty}$	Sh_m	average Sherwood number
E_a	the activation energy	T	Temperature
E_i	the estimated value	T_m	mean fluid temperature
$f(\eta)$	function on x component of flow velocity	$u\ , w$	flow velocity components
$\acute{f}(\eta)$	function on z component of flow velocity	z	axial coordinate
h	heat convection coefficient	**Greek symbols**	
h_{sf}	interstitial heat transfer coefficient	α	thermal diffusivity

k	thermal conductivity	β_h	nonlinear heat source parameter $\beta_h = \frac{Q_2.T_\infty}{Q_1}$
k^*	mean absorption coefficient	γ	modified conductivity ratio $\gamma = \frac{k_f}{k_s}$
k_c	chemical reaction rate constant	γ^*	Damköhler number $\gamma^* = \frac{k_R.a}{2D}\frac{1}{C_\infty}$
$\bar{k}$	freestream strain rate	X	input vector
k_1	permeability of the porous medium	η	similarity variable, $\eta = \left(\frac{r}{a}\right)^2$
k_m	mass transfer coefficient	$\theta(\eta)$	non-dimensional temperature
k_R	Kinetic constant	λ	Permeability parameter, $\lambda = \frac{a^2}{4k_1}$
k_T	thermal diffusion ratio	ε	Porosity
m	unit less exponent	σ^*	Stefan-Boltzmann constant
Q_h	heat source parameter $Q_h = \frac{Q_1.T_\infty.a^2}{4k_f}$	θ_w	Wall temperature parameter $\theta_w = \frac{T_w}{T_\infty}$
MAE	Mean Absolute Error, $MAE = \frac{1}{n}\sum_{i=1}^{n}(E_i - O_i)$	μ	dynamic viscosity
n	number of samples	υ	kinematic viscosity
N^*	dimensionless chemical reaction rate constant $N^* = \frac{k_c^2}{2\bar{k}}$	ρ	fluid density
Nu	Nusselt number	ϕ	non-dimensional fluid concentration
Nu_m	average Nusselt number	φ	angular coordinate
O_i	the observed value for the ith sample	**Subscripts**	
p	fluid pressure		
P	non-dimensional fluid pressure	w	Relate to the external wall of the cylinder
P_0	The initial fluid pressure	∞	far field
Pr	Prandtl number	f	Fluid
q_w	heat flux on the wall	s	Solid

1. Introduction

Fluid flow over a bluff body or on a stretching surface is widely encountered in nature and industry [1]. As a result, the stagnation point flow has received significant attention in classical hydrodynamics [2,3,4]. Polymer manufacturing [1], heat transfer and drying increment by impinging jets [5,6], subsiding zero-velocity regions of moving vehicles [7] and magnetorheological finishing process [8] are some technical instances of stagnation-point flow applications. There are, however, many situations that a stagnation-point flow is formed in porous media [9], such as packed bed heat exchangers, catalytic reactors and drying granular materials. Filling the porous media in micro-reactors containing highly exothermic reactions is a common way to increase heat transfer [10,11]. In particular, the chemical systems, including a stagnation-point flows over a curved body and surrounded by a porous material, are rarely touched. This could be because of the complex physics of this problem including solute diffusion, radiation and convection heat transfer, chemical reaction and hydrodynamics of stagnation flows [12]. Due to direct utilization of such systems in the industry, such as electrolysers [13] and thermochemical solar reactors [14], comprehensive understanding, optimization and simulation of them is an important necessity. Conventionally, porous-catalytic reactors are mostly modelled by assuming local thermal equilibrium [15,16], which treats a thermally homogenous mixture of fluid and solid [17]. However, existing strong heat source or sink and Soret and Dufour effects make this assumption invalid due to steep thermal gradients [18,19,20]. In the following, the limited existing works are briefly reviewed to demonstrate the-state-of-the-art in this field.

Chao et al. [21] took the first tangible steps in the problem including the stagnation-point flow, chemical reaction and catalytic porous bed. The governing equations were solved using conjugation of perturbation method and finite element approach. Higher temperature and lower reactant concentration were found as chemical reactivity increases or activation energy and solute diffusion rate decreased due to the higher conversion from

reactants to products. Sheri and Shamshudin [22] performed a boundary layer analysis on an unsteady chemically reactive flow past a plate made of porous materials. Radiation heat transfer, viscous dissipation and a magnetic field were assumed to be active. Increases in thermal radiative emissivity or absorption and viscous dissipation cause the thermal boundary layer to become thinner, while Prandtl number thickens it. Tlili et al. [23] analytically examined the velocity and thermal conditions of the non-Newtonian MHD flow on the stretching cylinder surrounded by the porous materials with chemical and thermal radiation effects. It was shown that convective heat transfer decreases with thermal slip, magnetic field, Reynolds number and solid volume fraction increment.

Pal and Biswas [24] analytically studied double-diffusive transport in an oscillatory flow over a plate in the porous medium using singular perturbation method. Increasing chemical reaction parameter led to concentration decrement and skin frictional coefficient increment. Convective and radiative heat transfer in an MHD stagnation-point flow on a stretched sheet embedded in a porous medium was investigated by Khan et al. [25,26]. The chemical reaction was also considered in the domain and the governing equations were reduced by the similarity method and then numerically solved. The base velocity profile was reduced by increasing Hartmann number, inertia factor and porosity parameter. Further, the temperature and concentration profiles were found to be mitigated as chemical reactive species, Prandtl number or Lewis number rises. Recently, Alizadeh et al. [27,28] investigated double diffusion of impinging flow on the cylinder in catalytic, porous media. The mathematical modelling included mixed convection, non-linear radiation and non-equilibrium thermal conditions to approach the real physics of the problem. In keeping with earlier works [22], they emphasized the dominant effects of Biot number on the Nusselt and Bejan number. Further, the non-equilibrium approach was declared to be essential for precise prediction in this problem.

Artificial neural network (ANN) is a method that restores the human brain process [29]. The structure of this method is emanated from the neural system, which requires input data, training process and output data, interconnected through multi-layers of information processing. This technique has recently been turned into the modern tool for optimization, prediction and analysis of complex and multi-functional engineering systems [30]. Making a comprehensive model from massive amount of data through taking conventional approaches is too complicated and ANN is a novel remedy [31]. Multiphase flow [32], aeronautics [33], turbulence [34] and fuel cells are the complex problems for which ANN has been successfully utilised for energy management.

Thermal engineering includes the wide range of problems that have been studied by this technique; prediction of heat transfer coefficient in internal flows of various types of heat exchangers [29] and external flows on hot bluff bodies [29] are some examples. This technique has been used for the heat and fluid flow in porous media. The optimum dimensions and material of the porous fins connected to the shell or tube side of the heat exchanger was determined using ANN by Ahmad et al. [35]. In another study, the effects of baffles cuts, permeability and porosity (inner layer) on the heat transfer rate (outer layer) was investigated through ANN by Mohammadi et al. [36]. Dealing with a multiphase flow through a porous media, Liu et al. [37] predicted the capillary pressure loss by ANN. The output data for various layers of the network was compared and it was found that it is different for each outer parameter.

Many problems in fluid mechanics feature a large number of inter-related parameters and therefore a conventional approach to their analysis will be very laborious and computationally intensive task. In such cases, machine-learning methods, such as ANN, can be used to predict the behavior of the problem without resort to extensive computations [38]. Clearly, the current problem requires a tool for low-cost modelling. Introducing the

large number of parameters, such as Reynolds, Dufour, Biot and Soret number as well as radiation parameter, reaction rate, permeability and porosity with multi-connection among them confirm that applying a non-linear, deep network approximation like ANN is a very reasonable approach to affordably predict the required outputs. Various types of ANN are examined to find a high-performance algorithm for the current problem and finally the radial basic function network is chosen. Non-linear radiative heat transfer, which was proved to make the prediction more accurate and improve the analysis [27] is utilized. Further, thermal non-equilibrium hypothesis that models the local heat transfer more accurately is applied [28].

2. Theoretical methods

2.1. The studied configuration, governing equations and assumptions

The schematic configuration of the current problem is shown in Fig. 1. An infinitely long cylinder coated by a layer of catalyst and surrounded by a fluid saturated porous medium is considered. The external surface of the cylinder is assumed to be made of the chemically reactive material of zeroth order and held at a fixed temperature. The fluid phase inside the porous medium hosts a homogenous, temperature dependent, chemical reaction. The uniform stagnation-point flow is formed on the cylinder, discussed later. Subscripts "s" and "f" in Eqs. (4) to (8) respectively indicate the solid and fluid phase.

The fluid flow and transport phenomena in this problem is described by the conservation of the mass, radial and axial momentum and energy, correspondingly presented in the following.

$$\frac{\partial(ru)}{\partial r} + r\frac{\partial w}{\partial z} = 0, \tag{1}$$

$$\frac{1}{\varepsilon^2}\left(u\frac{\partial u}{\partial r} + w\frac{\partial u}{\partial z}\right) = -\frac{1}{\rho}\frac{\partial p}{\partial r} + \frac{\upsilon}{\varepsilon}\left(\frac{\partial^2 u}{\partial r^2} + \frac{1}{r}\frac{\partial u}{\partial r} - \frac{u}{r^2} + \frac{\partial^2 u}{\partial z^2}\right) - \frac{\upsilon}{k_1}u, \tag{2}$$

$$\frac{1}{\varepsilon^2}\left(u\frac{\partial w}{\partial r} + w\frac{\partial w}{\partial z}\right) = -\frac{1}{\rho}\frac{\partial p}{\partial z} + \frac{\upsilon}{\varepsilon}\left(\frac{\partial^2 w}{\partial r^2} + \frac{1}{r}\frac{\partial w}{\partial r} + \frac{\partial^2 w}{\partial z^2}\right) - \frac{\upsilon}{k_1}w, \tag{3}$$

$$u\frac{\partial T_f}{\partial r} + w\frac{\partial T_f}{\partial z} = \alpha_f\left(\frac{\partial^2 T_f}{\partial r^2} + \frac{1}{r}\frac{\partial T_f}{\partial r} + \frac{\partial^2 T_f}{\partial z^2}\right) + \frac{h_{sf}.a_{sf}}{\rho.C_p}\left(T_s - T_f\right) + \left[Q_1\left(T_f - T_\infty\right) + Q_2\left(T_f - T_\infty\right)^2\right] + \frac{D\,k_T}{C_s.C_p}\left(\frac{\partial^2 C}{\partial r^2} + \frac{1}{r}\frac{\partial C}{\partial r} + \frac{\partial^2 C}{\partial z^2}\right). \tag{4}$$

The last term on the right-hand side of the energy equation (Eq.(4)) indicates transport of energy by diffusion mechanism of the mass, called Dufour effect [27,39]. Further, the energy conservation in the solid phase of the porous medium is governed by

$$k_s\left(\frac{\partial^2 T_s}{\partial r^2} + \frac{1}{r}\frac{\partial T_s}{\partial r} + \frac{\partial^2 T_s}{\partial z^2}\right) - h_{sf}.a_{sf}\left(T_s - T_f\right) - \frac{1}{r}\frac{\partial}{\partial r}(r.q_r) = 0. \tag{5}$$

Rosseland approximation [28,40] is used to determine the radiative heat flux as the following.

$$q_r = -\frac{4\sigma^*}{3k^*}\frac{\partial T_s^4}{\partial r}. \tag{6}$$

Applying Eq. (6), Eq. (5) can be re-arranged in the following nonlinear form

$$k_s\left(\frac{\partial^2 T_s}{\partial r^2} + \frac{1}{r}\frac{\partial T_s}{\partial r} + \frac{\partial^2 T_s}{\partial z^2}\right) - h_{sf}.a_{sf}\left(T_s - T_{nf}\right) + \frac{1}{r}\frac{\partial}{\partial r}\left(r.\frac{16\sigma^*}{3k^*}T_s^3\frac{\partial T_s}{\partial r}\right) = 0. \tag{7}$$

Considering a strongly temperature-dependent reaction rate and thermal diffusion of mass (Soret effects), the conservation of chemical species becomes [39,41,42]

$$u\frac{\partial C}{\partial r}+w\frac{\partial C}{\partial z}=D\left(\frac{\partial^2 C}{\partial r^2}+\frac{1}{r}\frac{\partial C}{\partial r}+\frac{\partial^2 C}{\partial z^2}\right)-k_c^2\left(\frac{T_f}{T_\infty}\right)^m e^{-\frac{E_a}{kT_f}}(C-C_\infty) + \frac{D\,k_T}{T_m}\left(\frac{\partial^2 T_f}{\partial r^2}+\frac{1}{r}\frac{\partial T_f}{\partial r}+\frac{\partial^2 T_f}{\partial z^2}\right). \tag{8}$$

The velocity boundary conditions applied to the momentum equations of (2) and (3) are presented as

$$r=a:\quad w=0\,,\quad u=0, \tag{9}$$

$$r=\infty:\quad w=2\bar{k}z\,,\quad u=-\bar{k}\left(r-\frac{a^2}{r}\right), \tag{10}$$

The current viscous flow approaches to the classical potential flow at the limit of $r\to\infty$ in Eq. (10) [6].
The thermal boundary conditions for the conservation of energy are presented by

$$\begin{aligned} r=a:&\quad T_f=T_w=\text{Constant},\\ &\quad T_s=T_w=\text{Constant},\\ r=\infty:&\quad T_f=T_\infty,\\ &\quad T_s=T_\infty, \end{aligned} \tag{11}$$

where T_w and T_∞ are correspondingly the cylinder surface and the free-stream temperature.
The mass transfer equation is closed by the following boundary conditions,

$$\begin{aligned} r=a:&\quad \frac{\partial C}{\partial r}=-\frac{k_R}{D}=\text{Constant},\\ r=\infty:&\quad C\to C_\infty, \end{aligned} \tag{12}$$

in which, k_R denotes the kinetic catalytic reaction constant of a zeroth order, D denotes the coefficient of molecular diffusion [43,44], and C_∞ is the mass concentration in the freestream flow.

2.2. Self-similarity

Applying the following similarity transformations,

$$u=-\frac{\bar{k}.a}{\sqrt{\eta}}f(\eta)\,,\qquad w=\left[2\bar{k}f'(\eta)\right]z\,,\qquad p=\rho_f\bar{k}^2a^2P, \tag{13}$$

where $\eta=\left(\frac{r}{a}\right)^2$ is the dimensionless radial coordinate, Eqs. (1) to (8) can be reduced to ordinary differential equations. Substituting Eq. (13) into the conservation of mass (Eq. (1)) directly satisfies it. This procedure for momentum equations of (2) and (3) leads to the following system of coupled differential equations.

$$\varepsilon^2\left[\eta f'''+f''+\frac{1}{4\eta}\frac{\partial^2 f'}{\partial\varphi^2}\right]+Re\left[1+ff'-\left(f'\right)^2\right]+\varepsilon^2.\lambda\left[1-f'\right]=0, \tag{14}$$

$$P-P_0=-\frac{1}{2\varepsilon^2}\left(\frac{f^2}{\eta}\right)-\frac{1}{\varepsilon}\left[\left(\frac{\acute{f}}{Re}\right)+\frac{\lambda}{Re}\int_1^\eta\frac{f}{\eta}d\eta\right]-2\left[\frac{1}{\varepsilon^2}+\frac{\lambda}{Re}\right]\left(\frac{z}{a}\right)^2 \tag{15}$$

In Eqs. (14) and (15), $Re = \frac{\bar{k}.a^2}{2\upsilon}$ shows the Reynolds number of the freestream flow, $\lambda = \frac{a^2}{4k_1}$ denotes the permeability parameter and prime symbol indicates derivative with respect to η. Eqs. (14) and (15) are bounded by the following reduced boundary conditions,

$$\eta = 1: \qquad f'(1) = 0\,, \qquad f(1) = 0, \tag{16}$$

$$\eta \to \infty: \qquad f'(\infty) = 1. \tag{17}$$

Aiding the following transformation [6, 27],

$$\theta_f(\eta) = \frac{T_f(\eta) - T_\infty}{T_w - T_\infty} \qquad , \qquad \theta_s(\eta) = \frac{T_s(\eta) - T_\infty}{T_w - T_\infty} \tag{18}$$

and substitution of Eq. (13) into Eq. (4), the energy equation can be rewritten in the non-dimensional form, which is

$$\eta\theta''_f + \theta'_f + Re.Pr.\left(f.\theta'_f\right) + Bi\left(\theta_s - \theta_f\right) + Q_h.\theta_f\left[1 + \beta_h.(\theta_w - 1)\theta_f\right] + \frac{Df.Pr}{\theta_w - 1}\left[\eta\phi'' + \phi'\right] = 0, \tag{19}$$

where $Q_h = \frac{Q_1.T_\infty.a^2}{4k_f}$ is the heat source parameter, $Df = \frac{D.k_T}{C_s.C_p}\frac{C_\infty}{\upsilon.T_\infty}$ is the Dufour number, $Bi = \frac{h_{sf}a_{sf}.a}{4k_f}$ is the Biot number and $\beta_h = \frac{Q_2.T_\infty}{Q_1}$ is the nonlinear heat source parameter. It should be noted that the dissipation terms are neglected in Eq. (19). The thermal boundary conditions reduce to

$$\eta = 1: \qquad \theta_f(1) = 1 \tag{20}$$

$$\eta \to \infty: \qquad \theta_f(\infty) = 0 \tag{21}$$

Similar procedure of non-dimensionalizing of fluid energy equation is performed for that of the porous medium, which leads to Eq. (22).

$$\eta\theta''_s + \theta'_s - Bi.\gamma\left(\theta_s - \theta_f\right) + R_d.\frac{\partial}{\partial\eta}\left[\eta.(1 + (\theta_w - 1)\theta_s)^3.\acute{\theta_s}\right] = 0, \tag{22}$$

where $\gamma = \frac{k_f}{k_s}$ is the modified conductivity ratio. The corresponding boundary conditions take the form of

$$\eta = 1: \qquad \theta_s(1) = 1, \tag{23}$$

$$\eta \to \infty: \qquad \theta_s(\infty) = 0. \tag{24}$$

Using the following transformation,

$$\phi(\eta) = \frac{C(\eta) - C_\infty}{C_\infty}, \tag{25}$$

the non-dimensional equation of mass transport (Eq. (8)) becomes

$$Pr\left[\eta\acute{\acute{\phi}} + \acute{\phi}\right] + Sr.Sc.(\theta_w - 1)\left[\eta\acute{\acute{\theta}}_f + \acute{\theta}_f\right] + Re.Pr.Sc\left(f.\acute{\phi}\right) - N^*.\phi.Re.Sc.Pr\left[1 + (\theta_W - 1)\theta_f\right]^m.e^{\frac{-E}{1+(\theta_W-1)\theta_f}} = 0 \tag{26}$$

In Eq. (26), $Sr = \frac{D.k_T}{T_m}\frac{T_\infty}{C_\infty.\alpha}$ is the Soret number, $Sc = \frac{\upsilon}{D}$ is Schmidt number, $N^* = \frac{k_c^2}{2\bar{k}}$ means a dimensionless chemical reaction rate, k_c^2 denotes the reaction rate constant, $\left(\frac{T_f}{T_\infty}\right)^m e^{-\frac{E_a}{kT_f}}$ indicates the modified Arrhenius

function, wherein k is the Boltzmann constant and m is a unitless exponent fitted rate constant and $E = \frac{E_a}{k.T_\infty}$ shows the non-dimensional activation energy. The non-dimensional mass boundary conditions are

$$\eta = 1: \qquad \acute{\phi}(1) = -\gamma^* = \frac{k_R.a}{2D}\frac{1}{C_\infty}, \tag{27}$$

$$\eta \to \infty: \qquad \phi(\infty) = 0. \tag{28}$$

Eqs. (14), (19), (22) and (26), in conjugation with the boundary conditions of (16),(17), (20), (21), (23), (24), (27) and (28) are solved numerically by employing an implicit, iterative, tri-diagonal finite-difference method [45].

2.3. Nusselt and Sherwood numbers

As the wall temperature is constant in the current problem, the local coefficient of convective heat transfer and its rate for the fluid phase are respectively taken by

$$h = \frac{q_w}{T_w - T_\infty} = \frac{-k_f\left(\frac{\partial T_f}{\partial r}\right)_{r=a}}{T_w - T_\infty} = -\frac{2k_f}{a}\frac{\partial \theta_f(1)}{\partial \eta}, \tag{29}$$

and

$$q_w = -\frac{2k_f}{a}\frac{\partial \theta_f(1)}{\partial \eta}T_w - T_\infty. \tag{30}$$

Nusselt number on the external surface of the cylinder is then given by

$$Nu = \frac{h.a}{2k_f} = -\acute{\theta}(1). \tag{31}$$

In a similar way, the local coefficient of mass transfer and the its rate are calculated as

$$k_m = \frac{q_m}{C_w - C_\infty} = \frac{-D\left(\frac{\partial C}{\partial r}\right)_{r=a}}{C_w - C_\infty} = -\frac{2D}{a}\frac{\partial \phi(1)}{\partial \eta}, \tag{32}$$

and

$$q_m = -\frac{2D}{a}\frac{\partial \phi(1)}{\partial \eta}C_w - C_\infty. \tag{33}$$

Sherwood number can be therefore determined by

$$Sh = \frac{k_m.a}{2D} = -\acute{\phi}(1). \tag{34}$$

2.4. Validation and grid independency

Before applying ANN, it should be shown that the numerical method employed to solve the governing equations can capture the real physics of the problem. The computational results from the set of equations are then fed to the ANN algorithm to fulfil the training procedure.

In the limit of very large values of porosity and permeability, meaning no porous medium and considering no mass transfer, the current numerical results are reduced to those of Wang [46] and Gorla [47], who studied the stagnation flow over a cylinder without any porous media. The comparison of velocity components and non-dimensional temperature is shown in Table 1. The average relative error between the results of the current study and those of Ref. [46] and [47] are lower than 0.1%. This is a confirmation to have a precise analysis in the current solution. In addition, though not shown here, it was concluded that in the limit of large value of Biot numbers in the porous medium, the results on the basis of current local thermal non-equilibrium (LTNE) and those of local thermal equilibrium (LTE) reported in Ref. [6], show no meaningful difference, as this is physically expected. These two comparisons present the validity of the chosen equations and numerical method. Further explanations of the employed numerical technique along with extensive validations can be found in the previous works of the authors [12,27,28].

To achieve the optimum grid size for performing the numerical solution, two non-dimensional dominant parameters, including the surface averaged values of Nusselt and Sherwood numbers were evaluated for different mesh sizes of 51×18, 102×36, 204×72, 408×144 and 816×288. The first and second number in mesh sizes indicate respectively the cells on the non-dimensional η and φ direction. As Table 2 shows, there is no considerable change in the results of the mesh sizes of (204×72), (408×144) and (816×288). Keeping the accuracy and affordability of the used mesh size, a (408×144) grid in $\eta - \varphi$ directions was selected for the computations conducted in the current work. Capturing the strong thermal and mass gradients in vicinity of the cylinder body, a non-uniform grid was implemented. The numerical procedure was stopped at any iteration that the residuals of algebraically discretized, governing equations become less than 10^{-7}, as the convergence criterion. All the discretization applied in the current numerical procedure is of accuracy of the second order, $O(\Delta\eta)^2$, recommended by the similar investigation [48].

2.5. Artificial Neural Network

Multilayer perceptron ANN is used in this study to predict output parameters, such as non-dimensional temperature of solid (θ_s), fluid (θ_f) and concentration (ϕ). This network contains several layers, typically called input, hidden and output, each one with some neurones. Fig. 2 shows a general structure of an ANN with n inputs, k hidden neurons and single output neuron. Every neurone connects to the other ones on the next layer through weight coefficient. The weights are optimized by back propagation of the error in the training stage across many iterations until the network is achieved to a desired accuracy. Here, an iteration or epoch indicates a complete forward-backward cycle and weight coefficient updates. The error of the algorithm prediction is evaluated through comparison against the benchmarking data [49].

2.5.1. Radial Basic Function network

Radial Basic Function (RBF) network is a type of neural network, specifically used for function estimation problems [50]. The RBF network, used in the current study, consists of three layers. Data are fed in the network

through the input layer. The second layer, or the hidden layer, contains the basic radial functions that the network name is derived from. The third layer is the output layer and contains sigmoid-like activation functions.

The input layer sends the data to the hidden layer without making any changes to them. The Gaussian function with the following equation is often used for the hidden layer,

$$h_i = \phi_i(X - \mu_i) = \exp\left(-\frac{\|X - \mu_i\|}{2\sigma_i^2}\right), \tag{35}$$

in which X is the input vector $(x_1, x_2, \dots, x_n)$ to the neural network. i is the hidden neuron index. μ_i and σ_i are center of region and width of the receptive field of neuron i, respectively.

The output layer is a linear combination of hidden functions. The connections between the hidden and output layers take weights that are actually the trainable parameters of the network. In other words, the input of the output layer neurons is the sum of the weighted radial basis functions shown in the following equation.

$$y = \sum_{i=1}^{k} w_i \, h_i(X). \tag{36}$$

There are two levels of learning for RBF network. Firstly, the center (μ) and spread (σ) of the middle layer neurons are determined. Different methods such as random [50], self-organized [51-52] and supervised [53-54] selection were tested to select centers. The self-organizing algorithm, which enables the RBF network to be automatically structured, is used in proposed models. Secondly, the weights of the output layer are learned. A common method for training RBF network weights is the error back propagation algorithm [51]. This algorithm simply updates the weights and biases in the direction in which the performance function strongly reduces. The algorithm iteration can be presented as

$$x_{k+1} = x_k - \alpha_k g_k, \tag{37}$$

where x_k is the current weights, g_k denotes the current gradient and α_k indicates the current learning rate.

2.5.2. Features methods

A method called Minimum Redundancy Maximum Relevance (MRMR) [52] is used to prioritize features in this study. This algorithm calculates the priority of each attribute, based on the value of the dependency on the target parameter and each member of the selected attribute set. The goal is to maximize the statistical dependency criterion with the target parameter and minimize the Mutual-Information (MI) among the set of selected variables. MI is calculated between the two features of x and y with the following equation, which is.

$$MI(x; y) = \iint p(x, y) \, log \frac{p(x)}{p(x)p(y)} dxdy. \tag{38}$$

In Eq. (38), $p(x)$, $p(y)$ and $p(x, y)$, respectively, are the probability density functions of the variables x, y, and their simultaneous occurrence.

One goal is maximizing the dependency of the set of selected features (S) on the target feature (h), mathematically meaning $\max(V_I(S,S))$ and presented by the following relation.

$$\max(V_I) = \max(\frac{1}{|S|}\sum_{i\in S} I(i,h)), \tag{39}$$

where V_I represents the value of the dependence of S on the h. Another goal is to create a minimum of redundancy by selecting a subset of features with the least correlation with each other, mathematically presented as $\min(W_I(S))$,. This is calculated by

$$\min(W_I) = \min(\frac{1}{|S|^2}\sum_{i,j\in S} I(i,j)), \tag{40}$$

in which W_I is the average MI between the features in subset S. By combining the two recent relations by $\varphi(V,W)$ operator, a concept is introduced as the Maximum Dependency Maximum Relationship (MRMR), which is $\max(\varphi(V,W))$, where φ is defined as

$$\varphi = V - W. \tag{41}$$

We used this method to prioritize features. In this regard, in each iteration of feature selection, the correlation value of each feature with the target feature is calculated. Also, the sum of the correlation value of each feature with the list of selected features before it is computed. Finally, by using the Eq. (41), the attribute, which has the highest correlation with the target and the least correlation with the previously selected features, is chosen.

also Mean Absolute Error (MAE) is the absolute value of the difference between the estimated value and actual value on average. MAE is calculated by following equation:

$$MAE = \frac{1}{n}\sum_{i=1}^{n}(E_i - O_i) \tag{42}$$

in which n is the number of samples, E_i and O_i are the estimated value and the observed value for the ith sample.

3. Results and discussion

The default values of the parameters used in the simulations is presented in Table 3. Figure captions, however, may report any deviation from these values. To select the appropriate method for estimating target parameters of ϕ and θ_f and θ_s, different models including MLP, Support Vector Regression (SVR) [53], Least Mean Square (LMS) [54] and RBF were tested. For this purpose, at first, the model inputs were prioritized by MRMR algorithm (see section 2.5.2). Then, the effect of increasing the number of features on the accuracy of the estimation model was measured using each model. The result of this experiment in estimating the parameter ϕ and θ_f are shown in Fig. 3. According to this figure, the RBF and MLP models present more accurate results. As the number of features increases, the accuracy of the RBF model is slightly improved compared with MLP model. Therefore, the RBF model was used in this research.

Fig. 4 shows the effects of Biot and Reynolds number on the dimensionless temperature distribution in fluid and solid. Considering a constant radial position, increasing Biot number leads to lower solid non-dimensional temperature, demonstrating higher absolute solid temperature. However, at the high Biot number values, the fluid remains with higher non-dimensional temperature and thicker thermal boundary layer. This emanates from the extracted heat from the solid phase at the limit of high Biot numbers. The temperature variation in the solid caused by Biot number changes is not as strong as that in the fluid, showing the importance of the convention heat transfer through the flow field. Increasing Reynolds number remains qualitative similar but more pronounced quantitative effects of decreasing Biot number. This figure illustrates that increasing Reynolds number diminishes the thermal boundary layer thickness by increasing the convection heat transfer. The fluid temperature variations, therefore, terminate at lower radial positions. The thermal boundary layer is more sensitive to the Reynolds number than Biot number through the studied range. Narrow radial variation of the temperature at higher Reynolds number is a reason to demonstrate similar trend in the solid temperature.

Introduction of radiation in the flow field can modify the temperature distribution, shown in Fig. 5. Surprisingly, the fluid temperature represents no function of radiation. This results from non-equilibrium thermal condition, which distinguishes the temperature of the fluid and solid, where the radiation heat transfer is implemented (see Eq. (7)). The solid temperature, however, reaches at the freestream temperature at lower radial distance only for the highest values of radiation parameter. This proves that the radiation heat transfer holds a threshold to affect the porous domain. The effect of wall temperature on the fluid and porous solid temperature distribution is depicted in Fig. 6. This figure shows that the temperature parameter plays a key role in the thermal response of the system. Increasing the wall temperature makes heat transfer stronger by forced convection and radiation. This causes the thermal boundary layer to become relatively thin by increasing the temperature parameter, such that η is 3.0 and 2.4, respectively for $\theta_w = 1.2$ and $\theta_w = 3.0$. The heated porous solid, however, is thicker due to lower thermal conductivity of the solid in comparison with the fluid flow (see Table 3 for $\gamma = 1.5$).

In contrast to the temperature, concentration represents accented dependency on the reaction rate, as Fig. 7 demonstrates. At the cylinder wall, increasing reaction rate leads to decreasing the non-dimensional concentration by one order of magnitude. This indicates that the higher reaction rate augments the generation of species on the surface of the catalyst [42], which is indicative of diminishing mass boundary layer. This figure also illustrates the effects of the Soret number values at different heat generation magnitudes on the mass distribution. Increasing heat generation aids the mass diffusion from the hot to the cold region at negative Soret number, as the mass boundary layer becomes finished at lower radial distances. This follows from the fact that heat transfer promotes the mass transfer for the negative Soret number values, while heat and mass transfer act in an opposite way for positive Soret numbers. The mass boundary layer, therefore, is thickened for the positive Soret numbers.

Fig. 8 shows the influences of Damköhler number and activation energy variation upon the concentration. Damköhler number increment leads to increasing the species production at non-zero activation energy. This is to be expected as the surface chemical kinetics accelerates by the increasing Damköhler number. Further away from the cylinder wall, the concentration approaches its value at the infinite radial position; however, this occurs at higher values of η and larger activation energy. Enhancing activation energy and Damköhler number has the same

effect on concentration. Non-dimensional concentration raises by the factor of three as the activation energy grows from zero to 50.

A monotonic increase in Nusselt number due to increasing the reaction rate, regardless of the value of heat source parameter, is seen in Fig. 9a. The slope of this increment increases at higher values of heat source strengths. The growth in heat source parameter features a strong influence on the Nusselt number increasing. This denotes that an increase in either heat source or reaction rate strength supports the convective heat transfer by aiding temperature difference. Nusselt number is not significantly influenced by the changes in Damköhler number. Fig. 9b shows that the Nusselt number increases with decreasing permeability of the porous medium, which has been reported in the previous works [56-61]. Soret number maximizes the Nusselt number at its negative value. Increasing the absolute value of Soret number can increase the thermal diffusion in comparison with the convection, resulting in decreasing the Nusselt number. Activation energy variation also holds the Nusselt number in a single-maximum trend. The Nusselt number shown in Fig. 9b and heat source parameter of $Q_h = 1$ at Fig. 9a indicates lower strength of convection in comparison with the conduction, as $Nu < 1$.

Figs. 10a and 10b depict the responses of Sherwood number to some functional parameters. Increasing heat source parameter increases heat convection (see Fig. 9) and subsequently enhances the mass transfer by the bulk flow, which can magnify Sherwood number. Increasing Damköhler number, indicating increasing the reaction rate, also magnifies the Sherwood number, gradually. Increasing activation energy of the chemical reaction intensifies the bulk mass transfer. Physically, increasing E decreases the modified Arrhenius function, endorsing a generative chemical reaction. In all studied cases through this figure, the mass diffusion is of greater importance than bulk mass transfer, evident by $Sh < 1$.

4. Conclusions

Artificial neural network (ANN) was used in the current study to predict the responses of temperature, concentration, Nusselt number and Sherwood number to the variations in the governing parameters. The radial basic function (RBF) network was chosen as the more precise and affordable algorithm for the problem of the flow past a superficially reactive cylinder embedded in a porous medium. RBF was selected after comparing various ANN models, such as multi-layer perceptron, support vector regression and least mean square. Considering non-equilibrium thermodynamics as well as non-linear radiation heat transfer aids the numerical simulation toward actual conditions. The numerical solution of the governing equations, reduced by semi-similarity technique, was performed through application of a finite difference technique. The obtained data were then employed to train the ANN. The key findings of the current study are in brief as follows:

- Increasing Biot number or decreasing Reynolds number results in thickening of thermal boundary layer.

- Dufour number increment postpones reaching the fluid temperature to the infinite temperature.

- Fluid temperature represents no dependency on the radiation heat transfer, while the solid temperature holds a threshold to respond to thermal radiation.

- No considerable temperature change is found through either chemical reaction rate or heat source variation.

- In contrast to the temperature, concentration is strongly affected by the reaction rate.

- Soret number increasing leads to Nusselt number rising at its negative value. Increasing the absolute value of Soret number can decrease the Nusselt number.

- Increasing Damköhler number, equivalently meaning increasing reaction rate, also magnifies the bulk mass transfer and Sherwood number.

- Increasing activation energy of the chemical reaction or Damköhler number enhances species production and strengthens the bulk mass transfer.

The current study demonstrated the capability of machine learning in aiding extensive parametric studies on the problems that involve a large number of parameters through reducing the required computation.

References

[1] Mahapatra, T.R. and Gupta, A.S., 2003, "Stagnation-point Flow towards a Stretching Surface," *Can. J. Chem. Eng.*, 81(2), pp.258-263.

[2] Dutta, B.K., Roy, P. and Gupta, A.S., 1985, "Temperature field in flow over a stretching sheet with uniform heat flux," *Int. Commun. Heat Mass Transfer*, *12*(1), pp.89-94.

[3] Wang, C.Y., 1984, "The three-dimensional flow due to a stretching flat surface," *Phys. Fluids*, **27**(8), pp.1915-1917.

[4] TC, C., 1994, "Stagnation-point flow towards a stretching plate," *J. Phys. Soc. Jpn.*, *63*(6), pp.2443-2444.

[5] Rohsenow, W.M., Hartnett, J.P. and Cho, Y.I., 1998, "*Handbook of heat transfer*," (Vol. 3). New York: McGraw-Hill.

[6] Alizadeh, R., Rahimi, A.B., Karimi, N. and Alizadeh, A., 2017, "On the hydrodynamics and heat convection of an impinging external flow upon a cylinder with transpiration and embedded in a porous medium," *Transp. Porous Media*, **120**(3), pp.579-604.

[7] Brimmo, A.T. and Qasaimeh, M.A., 2017, "Stagnation point flows in analytical chemistry and life sciences," *RSC Adv.*, **7**(81), pp.51206-51232.

[8] Kordonski, W.I. and Jacobs, S.D., 1996, "Magnetorheological finishing," *Int. J. Mod. Phys. B*, **10**(23n24), pp.2837-2848.

[9] Li, M., Wu, Y., Tian, Y. and Zhai, Y., 2007. "Non-thermal equilibrium model of the coupled heat and mass transfer in strong endothermic chemical reaction system of porous media," *Int. J. Heat Mass Transfer*, **50**(15-16), pp.2936-2943.

[10] Ting, T.W., Hung, Y.M. and Guo, N., 2015. "Entropy generation of viscous dissipative nanofluid flow in thermal non-equilibrium porous media embedded in microchannels," *Int. J. Heat Mass Transfer*, **81**, pp.862-877.

[11] Ting, T.W., Hung, Y.M. and Guo, N., 2015. "Entropy generation of viscous dissipative nanofluid convection in asymmetrically heated porous microchannels with solid-phase heat generation," *Energy Convers. Manage.*, **105**, pp.731-745.

[12] Alizadeh, R., Karimi, N., Arjmandzadeh, R. and Mehdizadeh, A., 2019. "Mixed convection and thermodynamic irreversibilities in MHD nanofluid stagnation-point flows over a cylinder embedded in porous media," *J. Therm. Anal. Calorim.*, **135**(1), pp.489-506.

[13] Pletcher, D. and Walsh, F.C., 2012. "*Industrial electrochemistry*," Springer Science & Business Media.

[14] Yadav, D. and Banerjee, R., 2016. "A review of solar thermochemical processes," *Renewable Sustainable Energy Rev.*, **54**, pp.497-532.

[15] Chein, R.Y., Chen, L.C., Chen, Y.C. and Chung, J.N., 2009. "Heat transfer effects on the methanol-steam reforming with partially filled catalyst layers," *Int. J. Hydrogen Energy*, **34**(13), pp.5398-5408.

[16] Chein, R.Y., Chen, Y.C. and Chung, J.N., 2012. "Thermal resistance effect on methanol-steam reforming performance in micro-scale reformers," *Int. J. Hydrogen Energy*, **37**(1), pp.250-262.

[17] Nield, D.A., Junqueira, S.L.M. and Lage, J.L., 1996. "Forced convection in a fluid-saturated porous-medium channel with isothermal or isoflux boundaries," *J. Fluid Mech.*, **322**, pp.201-214.

[18] Karimi, N., Agbo, D., Khan, A.T. and Younger, P.L., 2015. "On the effects of exothermicity and endothermicity upon the temperature fields in a partially-filled porous channel," *Int. J. Therm. Sci.*, **96**, pp.128-148.

[19] Torabi, M., Karimi, N., Zhang, K. and Peterson, G.P., 2016. "Generation of entropy and forced convection of heat in a conduit partially filled with porous media–local thermal non-equilibrium and exothermicity effects," *Appl. Therm. Eng.*, **106**, pp.518-536.

[20] Guthrie, D.G., Torabi, M. and Karimi, N., 2019. "Combined heat and mass transfer analyses in catalytic microreactors partially filled with porous material-The influences of nanofluid and different porous-fluid interface models," *Int. J. Therm. Sci.*, **140**, pp.96-113.
[21] Chao, B.H., Wang, H. and Cheng, P., 1996. "Stagnation point flow of a chemically reactive fluid in a catalytic porous bed," *Int. J. Heat Mass Transfer*, **39**(14), pp.3003-3019.
[22] Sheri, S. and Shamshuddin, M.D., 2018. "Finite element analysis on transient magnetohydrodynamic (MHD) free convective chemically reacting micropolar fluid flow past a vertical porous plate with Hall current and viscous dissipation," *Propuls. Power Res.*, **7**(4), pp.353-365.
[23] Tlili, I., Khan, W.A. and Khan, I., 2018. "Multiple slips effects on MHD SA-Al2O3 and SA-Cu non-Newtonian nanofluids flow over a stretching cylinder in porous medium with radiation and chemical reaction," *Results Phys.*, **8**, pp.213-222.
[24] Pal, D. and Biswas, S., 2018. "Magnetohydrodynamic convective-radiative oscillatory flow of a chemically reactive micropolar fluid in a porous medium," *Propuls. Power Res.*, **7**(2), pp.158-170.
[25] Khan, M., El Shafey, A.M., Salahuddin, T. and Khan, F., 2020. "Chemically Homann stagnation point flow of Carreau fluid," *Phys. A*, p.124066.
[26] Khan, M., Salahuddin, T., Malik, M.Y., Tanveer, A., Hussain, A. and Alqahtani, A.S., 2020. "3-D axisymmetric Carreau nanofluid flow near the Homann stagnation region along with chemical reaction: Application Fourier's and Fick's laws," *Math Comput Simul*, **170**, pp.221-235.
[27] Alizadeh, R., Karimi, N., Mehdizadeh, A. and Nourbakhsh, A., 2019. "Analysis of transport from cylindrical surfaces subject to catalytic reactions and non-uniform impinging flows in porous media," *J. Therm. Anal. Calorim.*, **138**(1), pp.659-678.
[28] Alizadeh, R., Karimi, N. and Nourbakhsh, A., 2019. "Effects of radiation and magnetic field on mixed convection stagnation-point flow over a cylinder in a porous medium under local thermal non-equilibrium," *J. Therm. Anal. Calorim.*, pp.1-21.
[29] Mohanraj, M., Jayaraj, S. and Muraleedharan, C., 2012. "Applications of artificial neural networks for refrigeration, air-conditioning and heat pump systems—A review," *Renewable Sustainable Energy Rev.*, **16**(2), pp.1340-1358.
[30] Ricardo, R.M., Manuel, H.L.J., Martín, D.G.H. and Arturo, P.V., 2014. "Use of artificial neural networks for prediction of convective heat transfer in evaporative units," *Ing., Invest. Tecnol.*, **15**(1), pp.93-101.
[31] Brunton, S.L., Noack, B.R. and Koumoutsakos, P., 2020. "Machine learning for fluid mechanics," *Annu. Rev. Fluid Mech.*, **52**, pp.477-508.
[32] Bahrami, B., Mohsenpour, S., Noghabi, H.R.S., Hemmati, N. and Tabzar, A., 2019. "Estimation of flow rates of individual phases in an oil-gas-water multiphase flow system using neural network approach and pressure signal analysis," *Flow Meas. Instrum.*, **66**, pp.28-36.
[33] Faller, W.E. and Schreck, S.J., 1996. "Neural networks: applications and opportunities in aeronautics," *Prog. Aeronaut. Sci.*, **32**(5), pp.433-456.
[34] Milano, M. and Koumoutsakos, P., 2002. "Neural network modelling for near wall turbulent flow," *J. Comput. Phys.*, **182**(1), pp.1-26.
[35] Ahmad, I., Zahid, H., Ahmad, F., Raja, M.A.Z. and Baleanu, D., 2019. "Design of computational intelligent procedure for thermal analysis of porous fin model," *Chin. J. Phys.*, **59**, pp.641-655.
[36] Mohammadi, M.H., Abbasi, H.R., Yavarinasab, A. and Pourrahmani, H., 2020. "Thermal optimization of shell and tube heat exchanger using porous baffles," *Appl. Therm. Eng.*, **170**, p.115005.
[37] Liu, S., Zolfaghari, A., Sattarin, S., Dahaghi, A.K. and Negahban, S., 2019. "Application of neural networks in multiphase flow through porous media: Predicting capillary pressure and relative permeability curves," *J. Pet. Sci. Eng.*, **180**, pp.445-455.
[38] Alanis, A.Y., Arana-Daniel, N. and Lopez-Franco, C. eds., 2019. "*Artificial Neural Networks for Engineering Applications*," Academic Press.
[39] Alizadeh, R., Gomari, S.R., Alizadeh, A., Karimi, N. and Li, L.K., 2019. "Combined heat and mass transfer and thermodynamic irreversibilities in the stagnation-point flow of Casson rheological fluid over a cylinder with catalytic reactions and inside a porous medium under local thermal nonequilibrium," *COMPUT MATH APPL*.
[40] Hayat, T., Waqas, M., Shehzad, S.A. and Alsaedi, A., 2016. "A model of solar radiation and Joule heating in magnetohydrodynamic (MHD) convective flow of thixotropic nanofluid," *J. Mol. Liq.*, **215**, pp.704-710.
[41] Abbas, Z., Sheikh, M. and Motsa, S.S., 2016. "Numerical solution of binary chemical reaction on stagnation point flow of Casson fluid over a stretching/shrinking sheet with thermal radiation," *Energy*, **95**, pp.12-20.
[42] Hunt, G., Karimi, N., Yadollahi, B. and Torabi, M., 2019. "The effects of exothermic catalytic reactions upon combined transport of heat and mass in porous microreactors," *Int. J. Heat Mass Transfer*, **134**, pp.1227-1249.

[43] Bhattacharyya, K., Mukhopadhyay, S., Layek, G.C. and Pop, I., 2012. “Effects of thermal radiation on micropolar fluid flow and heat transfer over a porous shrinking sheet,” *Int. J. Heat Mass Transfer*, **55**(11-12), pp.2945-2952.
[44] Torabi, M. and Aziz, A., 2012. “Entropy generation in a hollow cylinder with temperature dependent thermal conductivity and internal heat generation with convective–radiative surface cooling,” *Int. Commun. Heat Mass Transfer*, **39**(10), pp.1487-1495.
[45] Hussain, S.T., Haq, R.U., Noor, N.F.M. and Nadeem, S., 2017. “Non-linear radiation effects in mixed convection stagnation point flow along a vertically stretching surface,” *Int. J. Chem. React. Eng.*, **15**(1).
[46] Wang, C.Y., 1974. “Axisymmetric stagnation flow on a cylinder,” *Q. Appl. Math.*, **32**(2), pp.207-213.
[47] Gorla, R.S.R., 1993. “Mixed convection in an axisymmetric stagnation flow on a vertical cylinder,” *Oesterr. Ing.-Arch.*, **99**(1-4), pp.113-123.
[48] Thomas, J.W., 2013. “*Numerical partial differential equations: finite difference methods* (Vol. 22) ,” Springer Science & Business Media.
[49] Ahmadi, M.H., Ghazvini, M., Maddah, H., Kahani, M., Pourfarhang, S., Pourfarhang, A. and Heris, S.Z., 2020. “Prediction of the pressure drop for CuO/(Ethylene glycol-water) nanofluid flows in the car radiator by means of Artificial Neural Networks analysis integrated with genetic algorithm,” *Phys. A*, p.124008.
[50] Broomhead, D.S. and Lowe, D., 1988. “Multivariable functional interpolation and adaptive networks, complex systems,”vol. 2.
[51] Haykin, S., 2010. “*Neural Networks and Learning Machines, 3/E.*,” Pearson Education India.
[52] Peng, H., Long, F. and Ding, C., 2005. Feature selection based on mutual information criteria of max-dependency, max-relevance, and min-redundancy,” *IEEE Trans Pattern Anal Mach Intell*, **27**(8), pp.1226-1238.
[53] Drucker, H., Burges, C.J., Kaufman, L., Smola, A.J. and Vapnik, V., 1997. “Support vector regression machines,” Adv Neural Inf Process Syst .,pp. 155-161.
[54] Strutz, T., 2010, “Data Fitting and Uncertainty: A Practical Introduction to Weighted Least Squares and beyond,” Vieweg.
[55] Hunt, G., Karimi, N. and Torabi, M., 2018, “Two-dimensional analytical investigation of coupled heat and mass transfer and entropy generation in a porous, catalytic microreactor,” *Int. J. Heat Mass Transfer, , **119***, pp.372-391.
[56] Dickson, C., Torabi, M. and Karimi, N., 2016, “First and second law analysis of nanofluid convection through a porous channel-The effects of partial filling and internal heat sources,” *J. Appl. Therm. Eng.*, ***103***, pp.459-480.
[57] Torabi, M., Dickson, C. and Karimi, N., 2016. “Theoretical investigation of entropy generation and heat transfer by forced convection of copper–water nanofluid in a porous channel—local thermal non-equilibrium and partial filling effects,” *Powder Technol., , **301***, pp. 234-254.
[58] Wei Ting, T., Mun Hung, Y., and Guo, N. (2016). “Viscous dissipation effect on stream wise entropy generation of nanofluid flow in microchannel heat sinks,” ASME J. Energy Resour. Technol., **138**(5).
[59] Meng, X., & Yang, D., 2019, “Critical Review of Stabilized Nanoparticle Transport in Porous Media,” ASME J. Energy Resour. Technol., **141**(7).
[60] Zhao, W., Zhang, Y., Xu, B., Li, P., Wang, Z., & Jiang, S., 2018, “Multiple-relaxation-time lattice Boltzmann simulation of flow and heat transfer in porous volumetric solar receivers,” ASME J. Energy Resour. Technol., **140**(8).
[61] Papi, A., Mohebbi, A., and Ehsan Eshraghi, S., 2019, “Numerical Simulation of the Impact of Natural Fracture on Fluid Composition Variation Through a Porous Medium,” ASME J. Energy Resour. Technol., **141**(4).

Figures

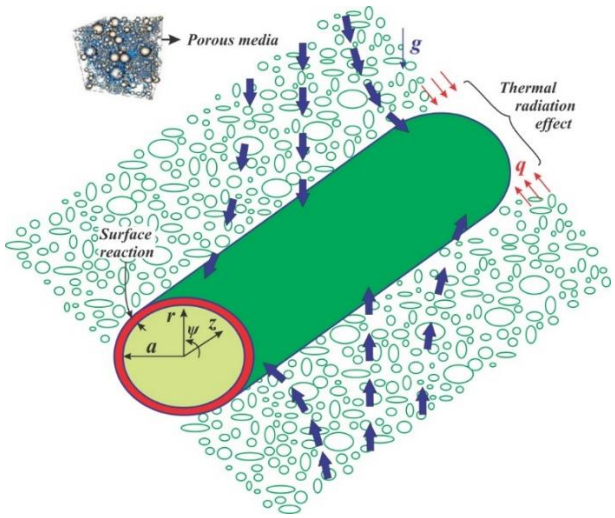

Fig. 1. Schematic view of a stationary cylinder under radial stagnation flow in porous media.

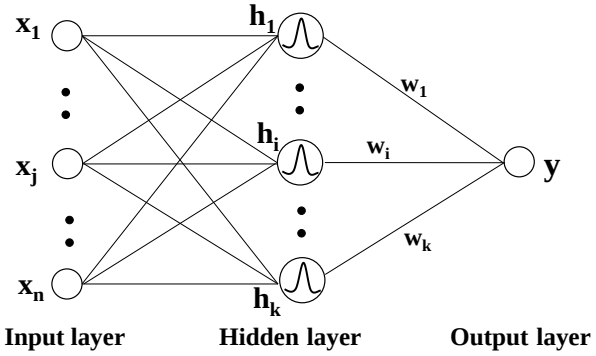

Fig. 2. Schematic view of a typical RBF network with n inputs, k hidden neurons and one output neuron.

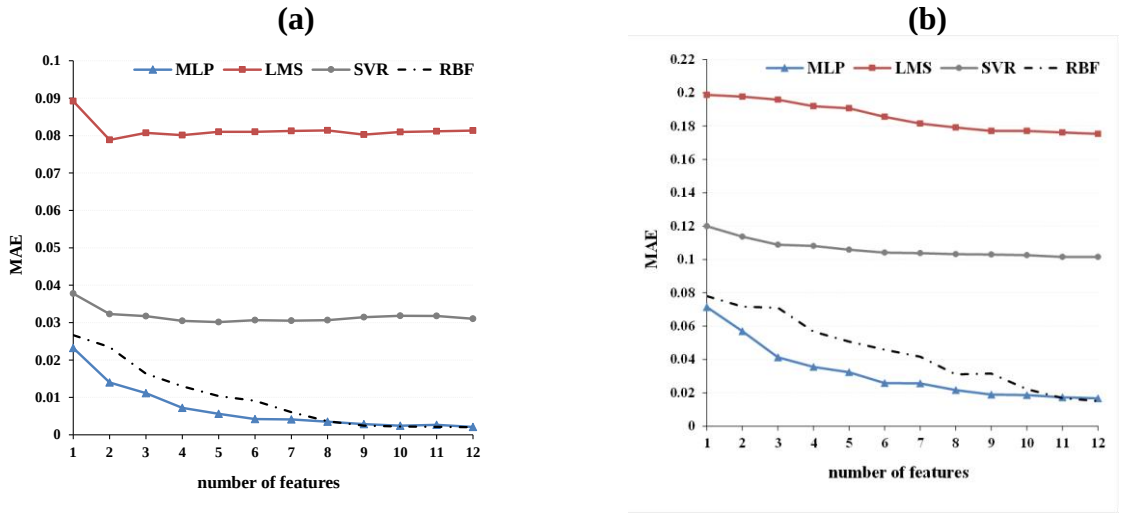

Fig. 3 The effect of increasing the number of features on the estimation model **(a)** concentration (ϕ) **(b)** fluid temperature (θ_f).

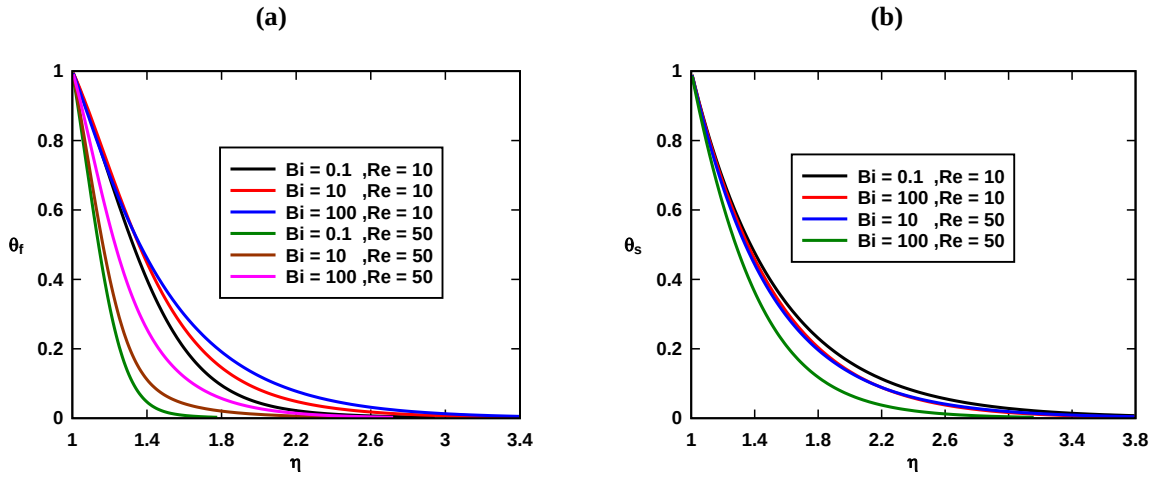

Fig. 4. Effects of Biot and Reynolds number on (a) $\theta_f(\eta)$ and (b) $\theta_s(\eta)$; $R_d = 10$, $Df = 1.0, Sr = 1.0$, $Sc = 0.1$, $\lambda = 10, \beta_h = 0, N^* = 10$, $m = 1.0, \gamma^* = 1.0, \theta_w = 1.5$.

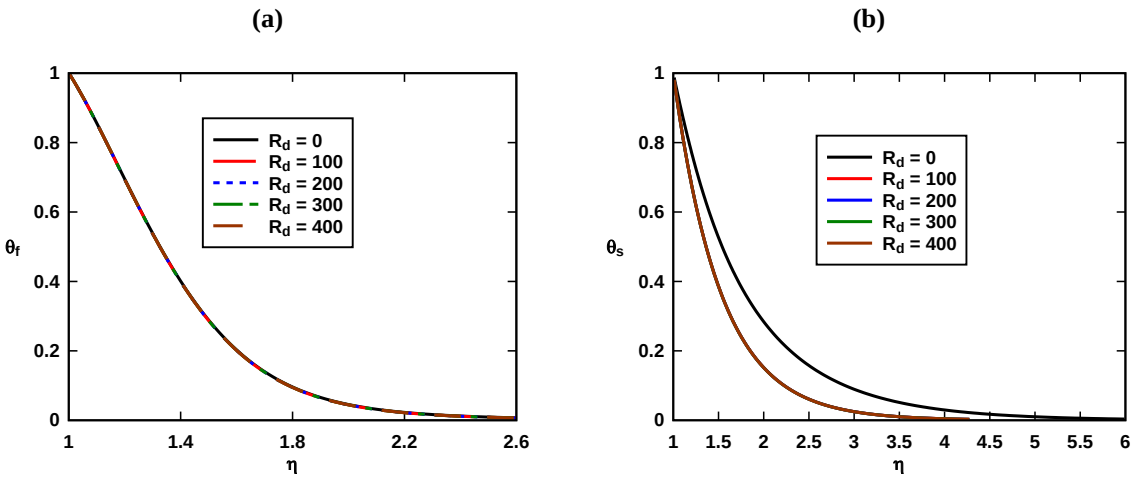

Fig. 5. Effects of radiation parameter on (a) $\theta_f(\eta)$,(b) $\theta_s(\eta)$, $Df = 1.0$, $Re = 10, Sr = 1.0$, $Sc = 0.1$, $\lambda = 10, \beta_h = 0, Q_h = 0, N^* = 10$, $m = 1.0, \gamma^* = 1.0, \theta_w = 1.5$.

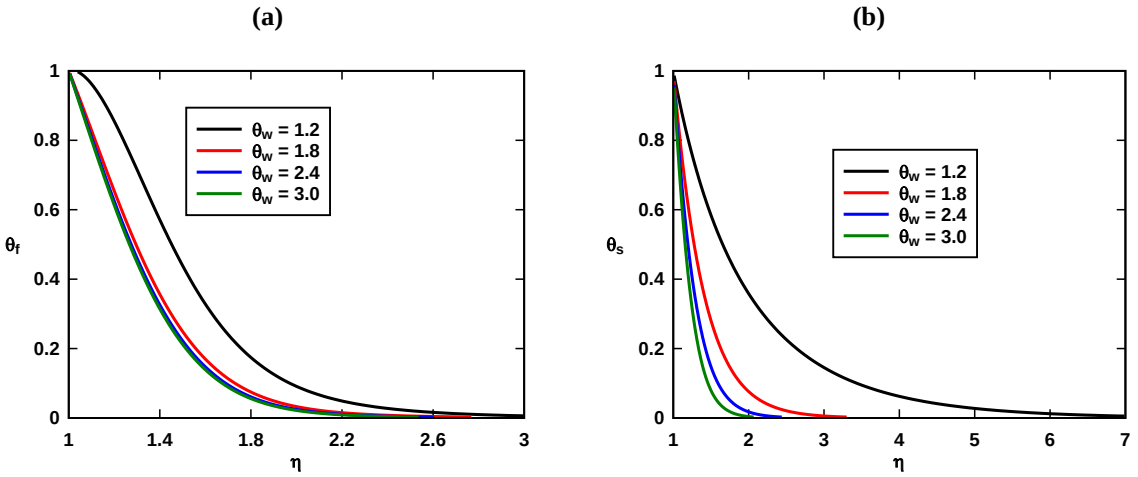

Fig. 6. Effects of wall temperature parameter on (a) $\theta_f(\eta)$,(b) $\theta_s(\eta)$, $R_d = 10$, $Re = 10, Sr = 1.0$, $Sc = 0.1$, $\lambda = 10, \beta_h = 0, Q_h = 0, N^* = 10$, $m = 1.0, \gamma^* = 1.0, Df = 1.0$.

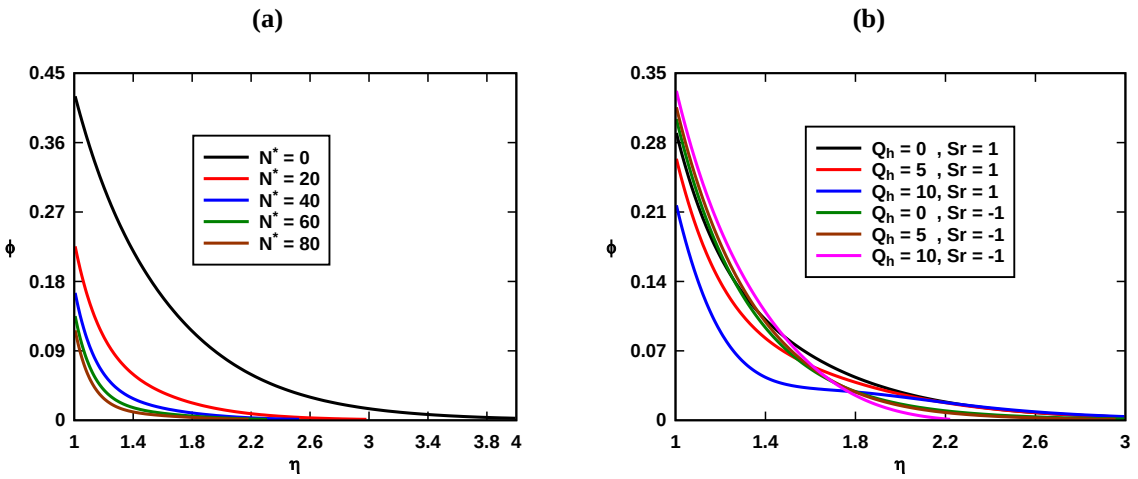

Fig. 7. Response of dimensionless concentration $\phi(\eta)$ to different values of (a) dimensionless chemical reaction rate constant,(b) Soret number, $R_d = 10\,, Re = 10, Sc = 0.1\,, \lambda = 10, \beta_h = 0, Q_h = 0\,, m = 1.0, \gamma^* = 1.0, \theta_w = 1.5$.

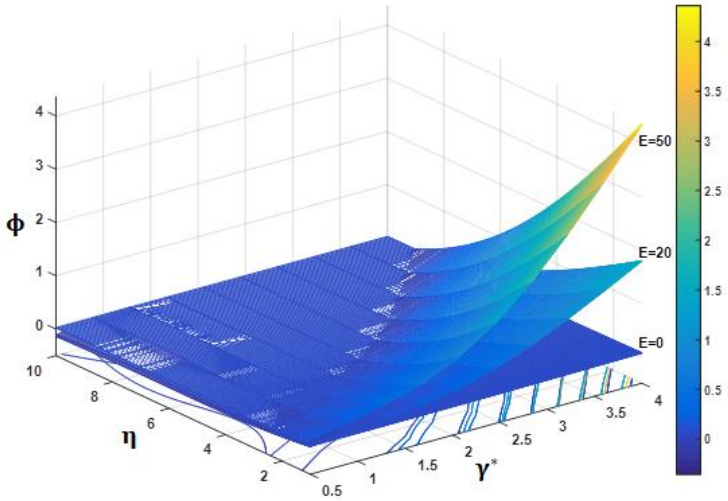

Fig. 8. Effects of non-dimensional energy of activation on dimensionless concentration $\phi(\eta)$, $R_d = 10\,, Re = 10, Sr = 1.0\,, Sc = 0.1\,, \lambda = 10, \beta_h = 0, Q_h = 0, N^* = 10\,, m = 1.0, \theta_w = 1.5$.

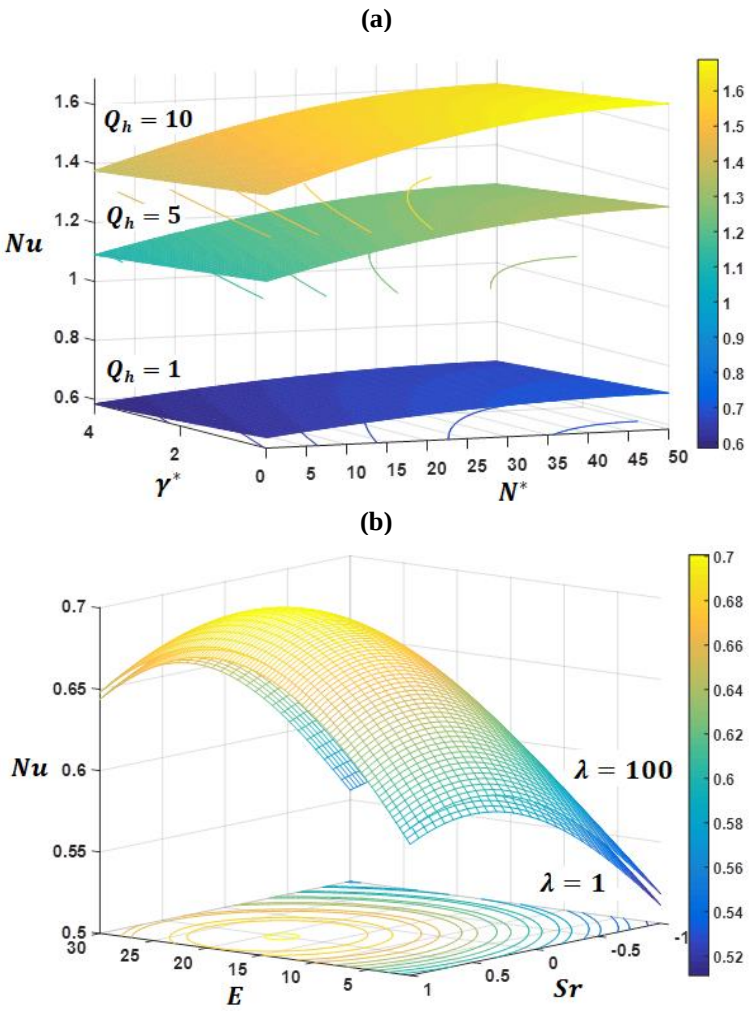

Fig. 9. Variation of Nu for different values of **(a)** heat source parameter **(b)** Permeability parameter $R_d = 10\,, Re = 10, Sr = 1.0\,, Sc = 0.1\,, \lambda = 10, \beta_h = 0, Q_h = 0, N^* = 10\,, m = 1.0, \theta_w = 1.5$.

(a)

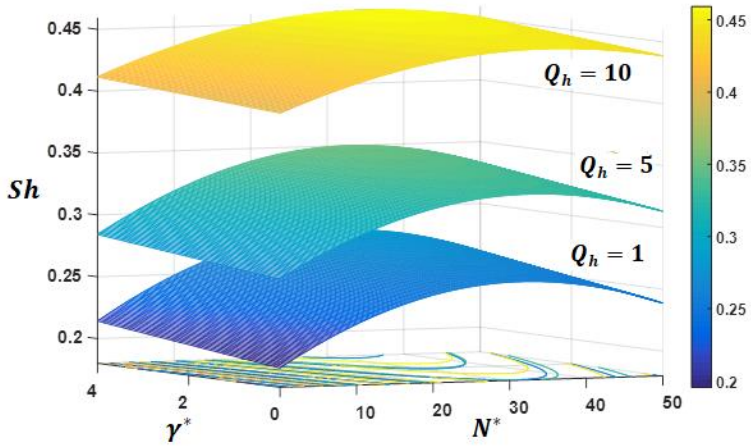

(b)

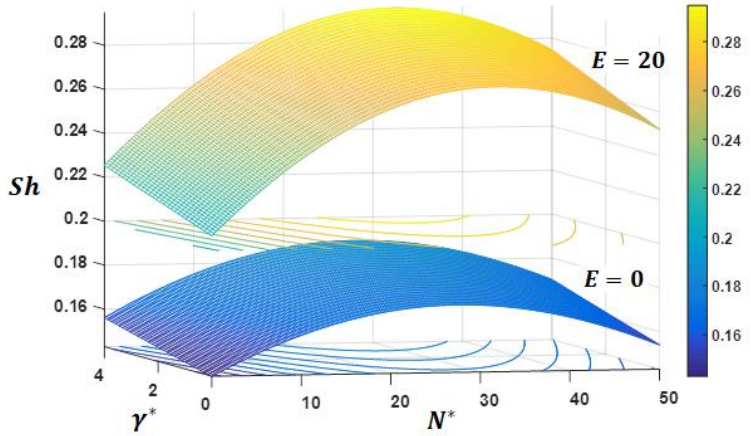

Fig. 10. Variation of Sh for different values of **(a)** heat source parameter **(b)** non-dimensional energy of activation, $R_d = 10$, $Re = 10, Sr = 1.0$, $Sc = 0.1$, $\lambda = 10, \beta_h = 0, Q_h = 0, N^* = 10$, $m = 1.0, \theta_w = 1.5$.

Tables

Table 1. Comparison between the current numerical results and those of Gorla [47] and Wang [46] in the limit of infinitely large porosity and permeability.

Re	f			θ		
	Gorla [47]	Current results	Relative Error (%)	Gorla [47]	Current results	Relative Error (%)
0.01	0.12075	0.12051	0.19	0.84549	0.84557	0.00
0.1	0.22652	0.22659	0.03	0.73715	0.73701	0.01
1.0	0.46647	0.46683	0.07	0.46070	0.46045	0.05
10	0.78731	0.78725	0.00	0.02970	0.02983	0.43
η	f			$\acute{f}$		
	Wang [46]	Current results	Relative Error (%)	Wang [46]	Current results	Relative Error (%)
1.2	0.02667	0.02693	0.97	0.25302	0.25993	2.73
1.4	0.09665	0.09652	0.13	0.43724	0.43710	0.03
1.6	0.19836	0.19828	0.04	0.57315	0.57329	0.02
1.8	0.32361	0.32365	0.01	0.67444	0.67438	0.00
2.0	0.46674	0.46683	0.01	0.75054	0.75046	0.01

Table 2. Surface mean Nusselt and Sherwood number for grid dependency test at $Df = 1.0$, $Bi = 0.1$, $Sr = 0.5$, $Re = 5.0$, $\lambda = 10$, $Sc = 0.1$.

Mesh size	Nu_m	Sh_m
51×18	0.691951	0.524891
102×36	0.652345	0.481365
204×72	0.614235	0.477389
408×144	0.604992	0.475422
816×288	0.604818	0.475290

Table 3. Default values of the simulation parameters

Simulation parameters	η	E	λ	ε	Re	Q_h	Bi	β_h	m	R_d	θ_w	γ	γ^*	N^*	Sr	Df
The default values	1.5	1.0	10	1.0	10	0	0.1	0	1.0	10	1.5	1.5	1.0	10	1.0	1.0